machines

MDPI

Article

An Anti-Singularity Data-Driven-Control-Based Method for Soft Start and Multi-Machine Balance of Magnetic Couplers

Yuqin Zhu [1,2], Wei Liu [1,*], Hongju Zhao [2,3], Chuang Yang [2,3] and Hao Liu [2,3]

1 School of Mechanical Engineering, Dalian University of Technology, Dalian 116023, China; zhuyq4005@mail.dlut.edu.cn
2 State Key Laboratory of Digital Intelligent Technology for Unmanned Coal Mining, Beijing 100013, China; zhaohj2020@126.com (H.Z.)
3 Science and Technology Innovation Center, Middling Coal Science and Industry Robot Technology Co., Ltd., Shenzhen 518000, China
* Correspondence: lw2007@dlut.edu.cn; Tel.: +86-131-3000-9890

Abstract

The speed-regulating magnetic coupler faces challenges in mechanism modeling for constant-torque-load soft start and multi-motor power balance. Moreover, system data contain singular noise values. To address these issues, an anti-singularity data-driven control strategy is proposed. This strategy enhances speed control accuracy and operational robustness. The method designs an exponentially stable air-gap regulation law using Lyapunov theory. A robust data model is constructed by estimating angular acceleration via piecewise least squares with singularity screening, followed by model extension using a generalized distance weighting factor, which enables the numerical solution of the control law. Experimental results demonstrate a speed control accuracy within 4%. In practical applications on long-distance belt conveyors, the strategy achieves a soft-start acceleration of $\leq 0.15\ \mathrm{m/s^2}$ with a 25 s start-up time, maintains power balance among motors within a 5% deviation, and improves energy efficiency by 17.6%. This work provides an effective data-driven solution for the high-performance control of magnetic couplers in complex industrial scenarios.

Keywords: magnetic coupling; speed control; model-free control; data-driven control; singularity

1. Introduction

The magnetic coupler transmits torque from the motor to the load and regulates speed by adjusting the air gap between the copper conductor and the permanent magnet. It offers advantages such as low requirements for alignment precision, high efficiency, and the capability for domestic substitution of imports at the MW level and above. Consequently, it is widely used in various industrial load transmission systems, including fans, water pumps, belt conveyors, and scraper conveyors [1–3].

Transportation equipment such as belt conveyors and scraper conveyors serves as core machinery in industrial production and mining operations. The permanent-magnet coupler is crucial for ensuring their operational stability, reliability, and high efficiency [4]. Belt conveyors and scraper conveyors are constant-torque loads. However, the mechanical characteristic of the coupler itself is similar to that of an induction motor, which exhibits a non-monotonic curve. Consequently, two intersection points exist when matched with a constant-torque load. This causes rapid load acceleration. It also leads to a sharp increase

Check for updates

Academic Editor: Ramani Kannan

Received: 6 January 2026
Revised: 30 January 2026
Accepted: 3 February 2026
Published: 26 February 2026

in starting speed after initiation. Furthermore, during speed regulation control, minor input variations often cause drastic fluctuations in output speed. These issues make it challenging to achieve S-curve soft start and power balance control in multi-motor drives and to establish an accurate mechanistic model. Conventional PID (Proportional–Integral–Derivative) controllers demonstrate poor speed regulation performance and low precision in air-gap control, failing to achieve soft starting for constant-torque loads or balanced power control in multi-motor systems. This results in issues such as drive shaft breakage and motor burnout due to direct start–stop operations under heavy-load starting conditions. Furthermore, in multi-motor drive systems like long-distance belt conveyors and scraper conveyors, uneven motor output and low operational energy efficiency are common. These inefficiencies reduce equipment service life. They also increase energy consumption during motor operation. These problems, particularly motor burnout and high energy loss, become even more pronounced in the application of MW-level and higher-power permanent-magnet couplers. To address these challenges, there is an urgent need for a precise, reliable, and stable control model and method to achieve soft start and multi-motor power balance regulation.

In traditional control systems, control can maintain the original performance of the system by minimizing the controller's sensitivity to model disturbances. When the model accuracy is too low, it will restrict the improvement of control performance [5]. Adaptive control can adjust controller parameters online to deal with system uncertainty. Likewise, the parameters of the recognizer or controller are difficult to converge with a low model accuracy [6]. Fuzzy control is designed with no controlled object model, and the control effect depends on manual experience [7]. Neural network control achieves parallel and distributed information processing function through network transformation and dynamic behavior. However, its reasoning process and reasoning basis have a black-box nature, and its reliability is relatively poor [8].

Data-driven control employs the input and output data for the controlled system, and it can realize the control of the equipment when it is difficult to establish the mechanism model of the controlled system [9,10]. As a typical data-driven control method, iterative learning control updates the control signal iteratively by sequentially applying the input–output data from previous runs, thereby enabling the system output to asymptotically approach the desired trajectory over repeated operations [11]. This method does not require an accurate mechanistic model of the system, but its effective application generally necessitates that the controlled process possesses repeatable operation characteristics [12]. Iterative learning control does not depend on the precise mathematical model of dynamic system, but requires repeatability of tasks and periodicity of interference [13]. Model-free adaptive control based on the dynamic linear data model of the controlled system is an adaptive control method. It overcomes the shortcomings of model-based adaptive control, such as high dependence on the system mechanism model, poor robustness, complex parameter identification mechanisms, and difficult controller design [14]. Model-free adaptive control highly depends on the input and output data of the system. In situations where system interference and measurement noise exist, corresponding data singularity processing measures are required to ensure the control performance [15,16].

Although data-driven methods such as iterative learning control (ILC) and model-free adaptive control (MFAC) provide effective frameworks for model-free control, they have limitations when applied to specific problems like controlling permanent-magnet couplers, which exhibit strong nonlinearity, contain singular noise in data, and involve non-repetitive operational tasks. ILC relies on task repetitiveness, while MFAC is typically based on locally linearized data models. Distinct from these frameworks, the proposed "anti-singularity data-driven control" method integrates three core ideas: (1) Introducing a singularity screening and limiting (SVSL) mechanism to specifically preprocess impulse noise and outliers in the data, enhancing data quality and robustness; (2) Employing a state-space memory model based on generalized distance weighting, which utilizes all historical operational data to extrapolate dynamic characteristics across operating points, strengthening nonlinear representation and generalization capability; (3) Tightly coupling the above data model with control law design based on Lyapunov stability, theoretically guaranteeing closed-loop exponential stability. This trinity design of "anti-interference data preprocessing–spatial memory model–stability theory" constitutes the unique innovation of our method, differentiating it from classical frameworks like ILC or MFAC.

This paper proposes an anti-singularity control method for permanent-magnet couplers based on the synergy between a Lyapunov stability framework and data-driven estimation. The controller equation is derived using Lyapunov stability theory. Indirect measurement of angular acceleration under interference and noisy environments is achieved by employing a piecewise least squares method with low-pass filtering characteristics and singular-point limiting functionality. The anti-singularity of the model is enhanced through data model extension based on a generalized distance weighting factor. The air-gap control output is obtained by solving the controller equation using this data model. Building upon this, a unified anti-singularity data-driven control system is constructed. This system specifically generates a trajectory tracking control strategy for S-curve soft starting of constant-torque loads and a distributed power balance coordination strategy for multi-motor drives. Experimental validation and practical engineering application were conducted. Through data-driven precise air-gap control, soft starting and energy-saving control via multi-machine power balance were achieved for heavy-duty equipment such as belt conveyors several kilometers in length.

2. Controller Design

The magnetic coupler changes the air gap by pushing the magnetic copper disk. This is achieved through gear–rack interaction between two disks. Then, the output torque and speed regulation can be realized.

As shown in (1), the output torque T of the magnetic coupler can be expressed as a binary function of speed n and air-gap control u. Under the condition of constant speed, the output torque increases while the air gap decreases [17].

$$\begin{cases} T = f(u,n) \\ T - T_0 = C_p a \\ a = \dot{n} \end{cases} \tag{1}$$

where T_0 is the minimum starting torque of the magnetic coupler, C_P is the rotational inertia of the output load, and a is the output angular acceleration.

The minimum start torque T_0 and load inertia C_P in (1) are independent of air-gap control value u and output speed n. Therefore, angular acceleration a can be expressed as a binary function of speed n and air-gap control value u

$$a = h(u,n) \tag{2}$$

and

$$\begin{cases} n_e = n_r - n \\ a_r = \dot{n}_r \end{cases} \tag{3}$$

where n_e is the rotational speed deviation, n_r is the set rotation speed, and a_r is the rate of change of the set rotation speed n_r with time.

From (1)~(3), the first time derivative of rotational speed deviation n_e is

$$\dot{n}_e = a_r - h(u, n) \tag{4}$$

The design of an exponentially stable air-gap regulation law begins with the choice of a suitable Lyapunov function candidate V. For the speed tracking error system described by (4), a quadratic Lyapunov function candidate in the form of $V = (1/2)e^2$ is selected, where $e = n_{ref} - n$ is the speed deviation. This choice is guided by the following criteria:

Positive Definiteness and Radial Unboundedness: $V(e) > 0$ for all $e \neq 0$ and $V(e) \to \infty$ as $|e| \to \infty$, which are fundamental requirements for proving global stability. Physical Interpretation: The function $(1/2)e^2$ represents the "energy" of the tracking error. Stabilizing the system equates to dissipating this error energy exponentially. Derivative Form Compatibility: The time derivative $\dot{V} = e\dot{e}$, when combined with the system dynamics (4), should lead to an expression where the control input u (air-gap) can be explicitly designed to ensure $\dot{V} \leq -\eta V$ with $\eta > 0$, thereby guaranteeing exponential convergence. Simplicity and Universality: The quadratic form is the most standard and effective candidate for first-order error dynamics, avoiding unnecessary complexity while providing a clear path to a stabilizing control law.

The Lyapunov function of rotation speed deviation n_e is constructed as follows

$$V(n_e) = {n_e}^2 \tag{5}$$

The first time derivative of Lyapunov function $V(n_e)$ can be obtained from (4) and (5)

$$\dot{V}(n_e) = 2n_e[a_r - h(u, n)] \tag{6}$$

According to Lyapunov stability criterion, the sufficient condition for asymptotic convergence of rotation speed deviation n_e in (4) is $\dot{V}(n_e) < 0$. Combined with (6), it can be seen that the rotational speed deviation n_e asymptotic convergence can be guaranteed by making (7) true. Equation (7) can be regarded as the equation of air-gap control quantity u

$$a_r - h(u, n) = -\eta n_e \tag{7}$$

where $\eta > 0$. Substituting (7) into (6) produces

$$\dot{V}(n_e) = -2\eta {n_e}^2 \tag{8}$$

Combining (5) and (8) produces

$$\dot{V}(n_e) = -2\eta V(n_e) \tag{9}$$

By solving (5) and (9), (10) can be obtained:

$$|n_e(t)| = |n_e(t_0)| exp(-\eta(t - t_0)) \tag{10}$$

where t_0 is the initial time. The exponential decay rate of the speed deviation n_e is $-\eta$.

3. Calculation of Angular Acceleration on the Sample Rail Line

3.1. Least Squares Linear Fitting

There is a strong nonlinearity between the torque, speed and air gap of the speed-regulating magnetic coupling, and it is difficult to establish a mechanism model. Therefore, in order to improve its speed control performance, a data model is necessarily established by its existing operating data.

The trajectory line formed by plotting the data of air-gap control amount u and output speed n corresponding to the operation process of the existing magnetic coupler on the $n-u$ plane is called the sample trajectory line, The points that make up the sample trajectory are called sample points.

The time series composed of $2q+1$ sample points is as follows: $n(k-q), n(k-q+1), \cdots, n(k+q-1), n(k+q)$.

The sequence is linearly fitted using the piecewise least squares method, and the slope calculation expression is

$$\dot{n}_e = a_r - h(u,n) \tag{11}$$

where $b(k,q)$ is the slope at time k calculated at $2q+1$ sample points.

The number of sample points used in (11) is $2q+1$. If the time interval between adjacent sample points is t_s, then the corresponding calculated values of time window width and angular acceleration are (12) and (13) respectively.

$$t_w = (2q+1)t_s \tag{12}$$

$$\hat{a}(k,q) = b(k,q)/t_s \tag{13}$$

where t_w is time window width and $\hat{a}(k,q)$ is the calculated value of angular acceleration.

3.2. Analysis of the Influence of Time Window Width and Signal Period on Bessel Phase Characteristic

As shown in Tables 1 and 2, by selecting different window widths and input signal cycles to detect the corresponding output, (11) can be obtained for the logarithmic amplitude gain and phase difference corresponding to different window widths and input signal cycles.

Table 1. Logarithmic amplitude gain (dB) under different signal periods and time window widths.

Signal Period $T/(s)$	**Window Width $t_w/(s)$**						
	0.615	**0.9925**	**1.23**	**1.845**	**2.46**	**3.69**	**4.92**
1/160	−2.1302	−4.8779	−9.7639	−38.9588	−21.6994	−29.0496	−4.3199
1/80	−0.6453	−1.2623	−2.1008	−4.9999	−9.5884	−41.2890	−21.1794
1/60	−0.4006	−0.7284	−1.1388	−2.6666	−4.9454	−12.9042	−42.1794
1/40	−0.3046	−0.4006	−0.4976	−1.1039	−1.9842	−4.8779	−9.5884
1/20	0.0690	−0.3046	−0.3046	−0.4006	−0.4006	−1.1039	−2.1008
1/10	0.5146	−0.0229	−0.0229	−0.2097	−0.4006	−0.3046	−0.5958

Table 2. Phase difference (dB) under different signal periods and time window widths.

Signal Period $T/(s)$	**Window Width $t_w/(s)$**						
	0.615	**0.9925**	**1.23**	**1.845**	**2.46**	**3.69**	**4.92**
1/160	−83.2331	−126.5414	−179.8421	−83.2331	−161.1880	−165.5188	−152.5263
1/80	−44.2556	−65.9098	−85.3985	−130.8722	−174.1805	−78.9023	−165.5188
1/60	−33.4286	−46.4211	−65.9098	−100.0150	−130.8722	−179.2105	−80.5263
1/40	−19.3534	−36.6767	−43.1729	−63.7444	−88.6466	−131.9549	−174.1805
1/20	−10.6917	−18.2707	−19.3534	−32.8872	−44.2556	−64.8271	−864,812
1/10	−6.0902	−7.7143	−12.3158	−17.7293	−21.7895	−33.1579	−42.6316

Draw intensity plots for Tables 1 and 2 as follows:

It can be seen from Tables 1 and 2 that the larger the time window width and the smaller the signal period, the larger the amplitude attenuation and the larger the phase lag.

The intensity plots corresponding to Table 1 and Table 2 are depicted in Figure 1a and 1b, respectively. Figure 1a visualizes the logarithmic amplitude gain, while Figure 1b shows the phase difference. Both plots intuitively demonstrate that the amplitude attenuation and phase lag increase with larger time window widths and smaller signal periods.

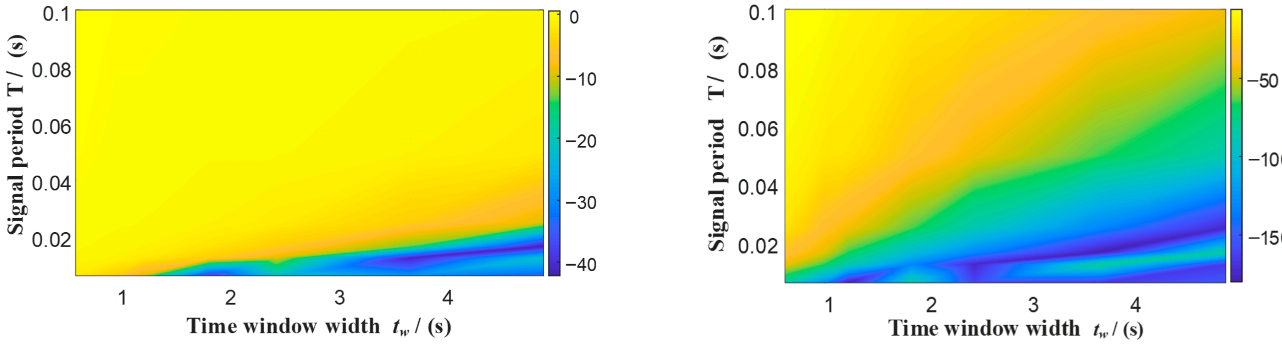

(**a**) Logarithmic amplitude gain (**b**) Phase difference

Figure 1. Bottom-two-fold-slope-fitting frequency characteristic intensity graph.

3.3. Singular-Value Screening and Limiting

In this section, a "singular point" refers to an outlier that severely deviates from the local data trend, quantified by the "singularity measure" in Equation (15). Screening is performed by iteratively calculating this measure for each point in the dataset, comparing it with a threshold (set to 1.0 r/min·s in experiments), and removing points whose measure exceeds the threshold, as outlined in Figure 2.

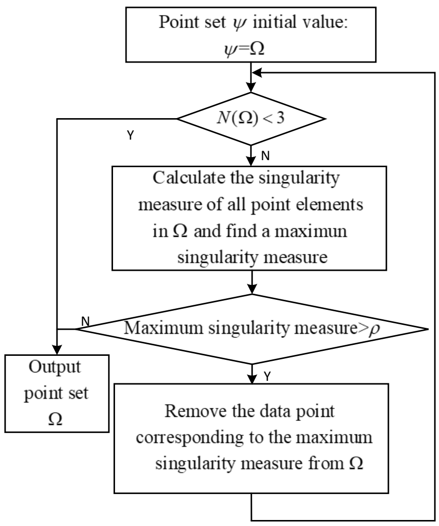

Figure 2. Flow chart of singular-value screening.

When the window width is small, singular points exist in the acceleration value obtained by least squares fitting [18]. In order to improve the accuracy of the mathematical model, it is necessary to screen and limit the singular points and establish a singularity measurement index to screen the singular points.

The point element of an instruction set Z is represented as $N(Z)$, the point elements are expressed as $(x_j, y_j), 1 \leq j \leq N(Z)$, and some elements of Z least squares linear fitting of slope $b_1(Z)$ and intercept $b_0(Z)$ expression are as follows:

$$\begin{cases} b_1(Z) = \dfrac{N(Z) \sum\limits_{(x_j,y_j)\in Z} x_j y_j - \sum\limits_{(x_j,y_j)\in Z} x_j \cdot \sum\limits_{(x_j,y_j)\in Z} y_j}{N(Z) \sum\limits_{(x_j,y_j)\in Z} x_j^2 - \left(\sum\limits_{(x_j,y_j)\in Z} x_j \right)^2} \\ b_0(Z) = \dfrac{1}{N(Z)} \sum\limits_{(x_j,y_j)\in Z} y_j - \dfrac{b_1(Z)}{N(Z)} \sum\limits_{(x_j,y_j)\in Z} x_j \end{cases} \tag{14}$$

The setpoint is Ω ($N(\Omega) \geq 3$), the point element is $(x_j, y_j), 1 \leq j \leq N(\Omega)$, and (x_i, y_i) is any point among them; let the set of remaining points after removing points (x_i, y_i) from Ω be Ω'. In (15), $\mu_i(\Omega)$ is called the singularity measure of the point (x_i, y_i) relative to the point set Ω.

$$\mu_i(\Omega) = \frac{1}{N(\Omega)} \sum_{(x_i,y_i)\in\Omega} (y_i - b_1(\Omega)x_j - b_0(\Omega))^2 - \frac{1}{N(\Omega')} \sum_{(x_j,y_j)\in\Omega'} (y_j - b_1(\Omega')x_j - b_0(\Omega'))^2 \tag{15}$$

The type of $b_1(\Omega)$, $b_0(\Omega)$, $b_1(\Omega')$, $b_0(\Omega')$ can be calculated according to the type (14).

The principle of singular-value screening is as follows: the singularity measures corresponding to all points in Ω are calculated. If the maximum singularity measure is greater than the judgment threshold, the data point corresponding to the maximum singularity measure is removed from Ω. A specific flow chart is shown in Figure 2.

In Figure 2, the value ρ of in the image is a threshold for judgment by the opposite sex.

Through the above methods, the points in Ω can be divided according to singularity; set Ω_A as nonsingular value point in Ω and Ω_B as collections of singular-value points in Ω. Set (x_j, y_j) as the point in Ω_B, namely $(x_j, y_j) \in \Omega_B$. Using (14), the valuation of the ordinate at x_j is

$$\hat{y}_j = b_1(\Omega_A)x_j + b_0(\Omega_A) \tag{16}$$

The singular-value screening and limiting (SVSL) can be solved by (17)

$$\begin{cases} y_j^* = \hat{y}_j + \rho, when\ y_j > \hat{y}_j + \rho \\ y_j^* = \hat{y}_j - \rho, when\ y_j < \hat{y}_j - \rho \end{cases} \tag{17}$$

where y_j^* the value of the singular-value y_j after amplitude limitation.

4. Calculation of Angular Acceleration in the Enclosed Area of the Sample Orbit

4.1. Numerical Solution for Air-Gap Control

Using the continuous smoothness of function $h(u, n)$, the closer the point (u, n) is to the sample point (u_i, n_i), the closer the calculated value of angular acceleration at the point (u, n) should be to the calculated value of angular acceleration at the sample point (u_i, n_i). The value of the angular acceleration of the points outside the track is obtained by the extension calculation. The extension calculation requires the distance between the sample point and the desired point.

Set the Euclidian distance between point (u, n) and point (u_i, n_i) as d_i in (18). The variable l_i that satisfies (19) is called generalized distance between point (u, n) and point (u_i, n_i).

$$d_i = \sqrt{(u - u_i)^2 + (n - n_i)^2} \tag{18}$$

$$\begin{cases} l_i > 0, when\ d_i \neq 0 \\ l_i = 0, when\ d_i = 0 \\ \frac{dl_i}{dd_i} > 0 \\ \lim\limits_{a_i \to \infty} l_i = +\infty \end{cases} \tag{19}$$

For any point (u,n) on the $n-u$ plane, the $e_i(u_i,n_i)$ in (20) is called the weighted factor of the sample point (u_i,n_i) to the point (u,n).

$$e_i(u,n) = \begin{cases} \frac{l_i^{-1}}{\sum_{j=1}^{j=N} l_j^{-1}}, l_j \neq 0, \forall j \in \{1,2,3,\cdots,N\} \\ 1, l_i = 0 \\ 0, l_j = 0, \exists j \in \{1,2,3,\cdots,N\}\ and\ j \neq i \end{cases} \tag{20}$$

where N is the number of sample points; l_i, l_j l_k are the generalized distance between sample points (u_i,n_i), (u_j,n_j) (u_k,n_k) and point (u,n) respectively.

The sum of the weighting factors of all sample point $(u_i,n_i), i=1,2,3,\cdots,N$ is 1; that is, (17) holds.

$$\sum_{i=1}^{i=N} e_i(n,u) = 1 \tag{21}$$

The classification of (20) is discussed as follows:

(1) When (u,n) does not coincide with all sample points, i.e.,

$$l_j \neq 0, \forall j \in \{1,2,\cdots,N\}$$

According to (20), it can be seen that

$$\sum_{i=1}^{i=N} e_i(u,n) = \sum_{i=1}^{i=N} \frac{l_i^{-1}}{\sum_{j=1}^{j=N} l_j^{-1}} = \frac{\sum_{i=1}^{i=N} l_i^{-1}}{\sum_{j=1}^{j=N} l_j^{-1}} = 1 \tag{22}$$

(2) When (u,n) coincides with any sample point (let point j the coincide), i.e.,

$$l_j = 1, l_k = 0, \forall k \in \{1,2,\cdots,N\}\ and\ k \neq j \tag{23}$$

According to (20), it can be seen that

$$\sum_{i=1}^{i=N} e_i(u,n) = \sum_{i=1}^{i=j-1} e_i(u,n) + e_j(u,n) + \sum_{i=j+1}^{N} e_i(u,n) = 1 \tag{24}$$

The angular acceleration value at the point can be calculated according to (25) by means of the angular acceleration value and the weighting factor on the sample rail line.

$$h^*(u,n) = \sum_{i=1}^{N} e_i(u,n) h(u_i,n_i) \tag{25}$$

where $h^*(u,n)$ is the angular acceleration value at the point (u,n) according to the angular acceleration at the sample points.

However, it is difficult to obtain the analytic expression of $h(u,n)$ in Equation (7). To calculate the value of air-gap control quantity u, Equation (7) can be solved through numerical calculation. The air-gap control amount in the current adjustment period was taken as the initial value, and the current speed was set as n_a. A solution satisfying

Equation (7) was searched in the neighborhood on both sides along the rotational speed line such as $n = n_a$ in the $n - u$ plane, as shown in Figure 3.

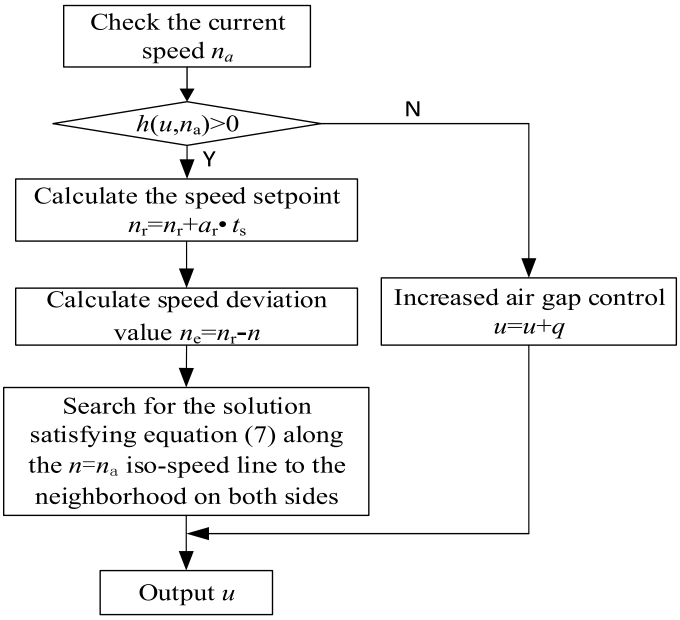

Figure 3. Flow chart of numerical solution for air-gap control.

4.2. Determination of the Generalized Distance Weighting Factor and Its Impact

The weighting factor $w_i(\lambda)$, defined in Equation (20), is the core mechanism for extending the angular acceleration model from the sample trajectory to the entire operating plane. Its determination is governed by two key aspects:

The Generalized Distance $\widetilde{d_i}$: It transforms the Euclidean distance d_i through the function $f(d_i) = d_i^{\lambda}$ (Equation (19)). The exponent λ is a critical design parameter that controls the "locality" of the weighting.

The Normalization: The weight $w_i(\lambda)$ for each sample point is obtained by normalizing the reciprocal of its generalized distance relative to all other sample points (Equation (20)). This ensures the principle that "closer points exert greater influence" and that the sum of all weights is 1 (Equation (21)).

The parameter λ directly dictates how sharply the influence of a sample point decays with distance: A small λ (e.g., $\lambda \to 0$) makes the weights nearly uniform, leading to over-smoothed extrapolation that fails to capture local nonlinearities. A large λ (e.g., $\lambda \geq 5$) causes the weight to be dominated by the single nearest sample point, resulting in a piecewise-constant extrapolated model that is prone to discontinuous jumps and poor generalization. A moderate λ achieves a balanced trade-off, allowing multiple nearby samples to contribute meaningfully while respecting distance-based relevance.

Impact on Model Extension Effectiveness: The effectiveness of the model extension—its ability to provide accurate and physically plausible acceleration estimates across the (x/n) plane—is highly sensitive to λ. An appropriately chosen λ ensures the following: Smoothness: The extrapolated acceleration field varies continuously, avoiding artificial discontinuities. Fidelity to Local Dynamics: The model retains the nonlinear characteristics observed near the sample trajectories. Robustness to Sparse Sampling: It reasonably interpolates or extrapolates in regions distant from sample points without wild oscillations.

5. Implementation of Anti-Singularity Data-Driven Control System

To apply the aforementioned theoretical models and algorithms to the practical speed control of magnetic couplers, this chapter constructs a complete anti-singularity data-driven control system and elaborates on its specific implementation strategies for constant-torque-load soft start and multi-motor power balance regulation. The core of the system lies in utilizing the data-driven model to estimate system dynamics in real time and computing the optimal air-gap control variable online by solving the control law derived from Lyapunov theory.

5.1. System Architecture and Workflow

Based on the theoretical derivations from Sections 2–4, the overall architecture of the constructed anti-singularity data-driven control system is shown in Figure 4. Its core is the closed-loop solution of the air-gap regulation law through the data model.

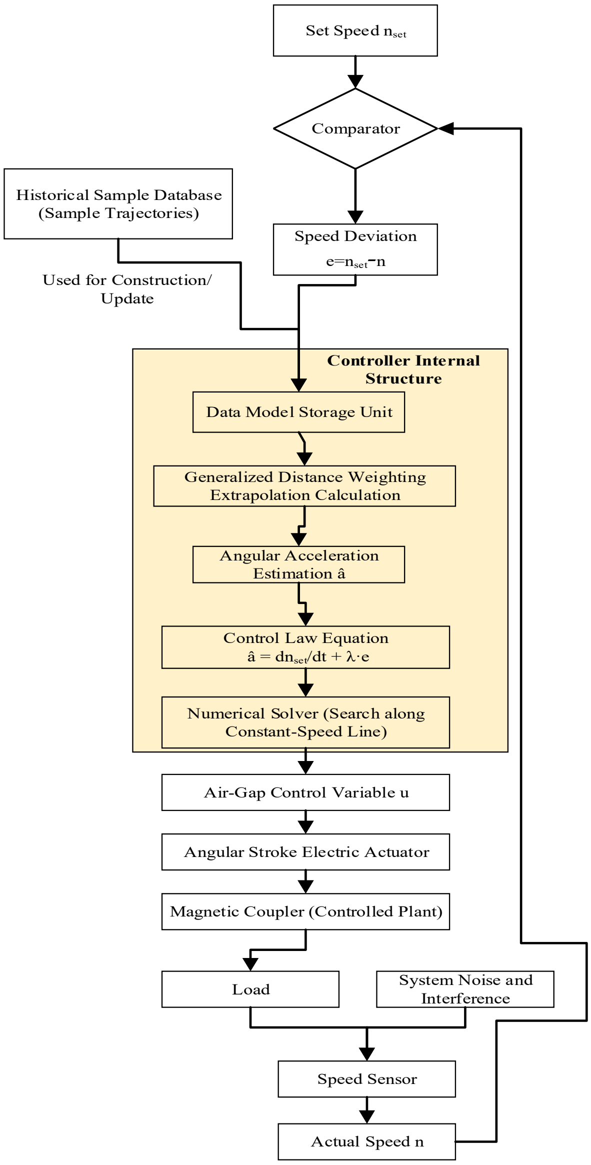

Figure 4. Block diagram of the anti-singularity data-driven control system architecture.

This figure illustrates the complete closed-loop architecture of the anti-singularity data-driven control system. The system takes the set speed n_{set} as input and compares it with the actual speed n to generate the speed error e. This error, along with the speed derivative, is fed into the anti-singularity data-driven controller. The controller core consists of two interlinked modules: the data model storage unit (based on historical sample trajectories) and the numerical solver. First, the generalized distance weighting extrapolation algorithm is used to estimate the angular acceleration $\hat{a}$ in real time from the data model based on the current operating point $(n'u)$. Subsequently, $\hat{a}$ is substituted into the control law equation derived from Lyapunov stability, and the numerical solver searches along the current constant-speed line to compute the optimal air-gap control variable u. This control variable drives the angular stroke electric actuator to adjust the magnetic coupler, changing the air gap to regulate the torque transmitted to the load, ultimately achieving precise speed tracking. The load speed is detected by the speed sensor and fed back, forming a closed loop. Noise and disturbances present in the system are indicated at the sensor stage, while the SVSL algorithm proposed in this paper is embedded within the data model construction and acceleration estimation process, ensuring the controller's anti-interference capability.

The system operates according to the following workflow within each control cycle k:

Data Acquisition and Mapping: Sample the load speed $n(k)$ and the current air-gap control variable $u(k-1)$ in real time. Map the point $P(k) = (n(k), u(k-1))$ to the $n - u$ plane.

Data Model Query and Acceleration Estimation: Using $P(k)$ as the query point, estimate the angular acceleration $\hat{a}(k)$ at the current point from the pre-established sample trajectory data model $\mathcal{M}$ based on the generalized distance weighting extrapolation algorithm proposed in Section 3.3. The calculation synthesizes Equations (20) and (25):

$$\hat{a}(k) = \sum_{i=1}^{N_s} \omega_i(k) \cdot \alpha_i \tag{26}$$

where $\omega_i(k)$ is the weight of the *i-th* sample point $S_i = (n_i, u_i)$ relative to the query point $P(k)$, calculated according to Equation (20); α_i is the angular acceleration value at sample point S_i after processing by singular-value screening and limiting (Section 3.3). This step achieves a data-driven approximation of the system's nonlinear dynamics $\alpha = f(n, u)$.

Control Law Calculation: Calculate the current speed error $e(k) = n_{set}(k) - n(k)$ and its rate of change. Substitute $\hat{a}(k)$, $e(k)$, and the Lyapunov coefficient λ into the air-gap regulation law equation defined by Equation (7):

$$\hat{a}(k) = \dot{n}_{set}(k) + \lambda e(k) \tag{27}$$

Note that $\hat{a}(k)$ replaces the theoretical value $a(k)$ here.

Numerical Solution for Air-Gap Control Variable: Using $u(k-1)$ as the initial guess, employ the numerical search algorithm shown in Figure 3 of Section 4 along the current constant-speed line $n = n(k)$ to solve the equation $f_{data}(n(k), u) = \hat{a}(k)$, obtaining the optimal air-gap control variable $u^*(k)$ that satisfies the accuracy requirement. Here, $f_{data}(\cdot)$ represents the functional relationship described by the data model $\mathcal{M}$.

Control Output and Execution: Output $u^*(k)$ to the angular stroke electric actuator, which drives the magnetic coupler to adjust the air gap to the target position, thereby changing the torque transmitted to the load and completing one closed-loop control cycle.

This architecture combines Lyapunov stability theory with data-driven modeling. Through real-time data querying and numerical solutions, it avoids dependence on complex mechanistic models and ensures the controller's robustness against noise and interference via anti-singularity processing.

5.2. Implementation of Soft-Start Control Strategy for Constant-Torque Loads

For constant-torque loads such as belt conveyors and scraper conveyors, direct starting generates significant mechanical and electrical shock. The proposed method achieves soft start by planning and accurately tracking a smooth start-up speed curve [19].

https://doi.org/10.3390/machines14030263

Start-up Curve Planning: Based on the total load inertia J and the permitted maximum start-up acceleration $a_{\max}$ (e.g., $\leq 0.15\ \mathrm{m/s^2}$), design an S-shaped (Sigmoidal) speed setpoint curve $n_{set}(t)$. Its mathematical expression can be represented as

$$n_{set}(t) = n_{final} \cdot \left(\frac{1}{1+e^{-k_s(t-t_0)}} - \frac{1}{1+e^{k_s t_0}}\right) \cdot \frac{1+e^{k_s t_0}}{e^{k_s t_0}} \tag{28}$$

where n_{final} is the target speed, k_s is the curve smoothing factor, and t_0 is the curve center offset. The acceleration of this curve approaches zero at the beginning and end of the start-up, the maximum acceleration is limited within the permissible range, and the total start-up time is extended to T_{start} (e.g., 25 s).

Closed-Loop Tracking Control Process: The control system takes $n_{set}(t)$ as the setpoint and executes the closed-loop process described in Section 5.1.

At the start instant ($t = 0$), the air gap is at its maximum; consequently, the transmitted torque is very small, and the load is either stationary or running at low speed.

Based on the deviation between the current speed $n(k)$ and the setpoint value $n_{set}(k)$, the controller solves Equation (27) to obtain the air-gap adjustment variable $u^*(k)$ that ensures exponential convergence of the system.

The actuator drives the air gap to decrease and the transmitted torque $T(n,u)$ increases accordingly (Equation (1)), driving the load to accelerate.

Throughout the start-up process, the data model $\mathcal{M}$ can accurately estimate the acceleration $\hat{a}$ under different $(n'u)$ combinations, enabling the controller to "sense" in advance the impact of air-gap adjustment on dynamics. Consequently, it calculates smooth air-gap change commands, ultimately enabling the load speed to perfectly track the S-shaped curve and achieve the soft-start goal of "smooth speed, minimal shock".

5.3. Implementation of Multi-Motor Drive Power Balance Control Strategy

In scenarios where multiple motors jointly drive a single load (e.g., a long-distance belt conveyor), uneven motor output leads to increased equipment wear and reduced efficiency. This control strategy achieves dynamic power balance by coordinately adjusting the air gaps of the magnetic couplers on each drive branch [20–22].

Power Balance Principle and Objective: Assume the system has m drive motors, with a total load power of P_{load}. Ideally, each motor should share the load proportionally according to its rated capacity. Define the actual output power of the j-th motor as P_j, and its desired allocated power as $P_{j,des}$. The control objective for power balance is to minimize the power deviation of each motor:

$$\min \sum_{j=1}^{m} \left| P_j - P_{j,des} \right| \tag{29}$$

Since motor power is strongly correlated with current, the motor stator current I_j is used as the observation index for power balancing in practice.

Distributed Coordinated Control Strategy: The system periodically detects the currents $I_1, I_2, \cdots, I_m$ of each motor.

Balance Judgment: Calculate the average current $I_{avg} = \frac{1}{m}\sum_{j=1}^{m} I_j$ and the current deviation of each motor $\Delta I_j = I_j - I_{avg}$. If $\max(|\Delta I_j|) > \delta_{th}$ (threshold, e.g., corresponding to 5% power imbalance), balance regulation is triggered.

Inverse Adjustment Logic: For motors with current higher than the average (excessive output), the air gap u_j of its magnetic coupler should be increased to reduce the transmitted torque, thereby decreasing the output current. For motors with current lower than the average (insufficient output), the air gap u_j should be decreased to increase torque and current.

Independent Closed-Loop Calculation: The air-gap adjustment amount Δu_j for each motor is independently calculated by its own anti-singularity data-driven controller. This controller has the implicit goal of "adjusting I_j to I_{avg}" but directly controls the speed. Its set speed n_{set} remains the common system value. The controller solves for the new air-gap control variable u_j^* based on the deviation between its local speed n_j and the common setpoint, as well as the dynamics estimated by its local data model. Due to the mechanical coupling of the motors, adjusting the torque of one motor slightly affects the common speed, which in turn triggers responses from other controllers. Through this distributed coupling, the output of all motors eventually converges to a balanced state.

Convergence and Stability: Since each branch controller is designed based on Lyapunov stability, single-loop stability is guaranteed. The coordination process can be viewed as dynamic coupling between multiple stable loops. Experiments show that this system can converge to the equilibrium point rapidly.

Through the above strategies, the proposed anti-singularity data-driven control method, starting from a unified algorithmic framework, generates two application modes: time trajectory tracking control for soft start and multi-loop coordinated control for multi-motor balance, fully demonstrating its flexibility and effectiveness. The following experimental chapter will validate the actual performance of these two functions.

5.4. Robustness Discussion

The proposed control system integrates Lyapunov-based theoretical design with data-driven online estimation. A natural question is whether the data model estimation error $\Delta\alpha$ and numerical approximation might compromise the system's stability guarantees. This subsection provides an analysis.

The closed-loop speed error dynamics can be expressed as $\dot{e} = -ke + \Delta\alpha$, where the term $-ke$ is guaranteed by the Lyapunov design, and $\Delta\alpha = \hat{\alpha} - \alpha$ is the angular acceleration estimation error. This equation reveals that the system possesses Input-to-State Stability (ISS) properties with respect to the matched disturbance $\Delta\alpha$: as long as $\Delta\alpha$ is bounded, the speed tracking error e is also necessarily bounded. The control gain k governs both the error convergence rate and the attenuation capability against the disturbance $\Delta\alpha$.

The data-driven components in this work are designed precisely to actively manage $\Delta\alpha$: (1) Singular-value screening and limiting (SVSL) suppresses impulse noise outliers in the data, significantly reducing the instantaneous peak of $\Delta\alpha$; (2) Generalized-distance-weighted extrapolation aims to improve the estimation accuracy of $\hat{\alpha}$, thereby reducing the persistent magnitude of $\Delta\alpha$. The minor error introduced by numerical solution can be viewed as a bounded actuator of input disturbance. For a stable closed-loop system, such a disturbance leads only to bounded output deviation without causing instability.

In summary, the system design acquires an inherent robustness framework against disturbances through Lyapunov theory and proactively constrains and reduces the magnitude of the primary disturbance source ($\Delta\alpha$) via targeted data processing. This dual approach jointly ensures the robust stability of the closed-loop system from both theoretical and practical perspectives.

5.5. Computational Complexity and Real-Time Feasibility

The proposed anti-singularity data-driven control algorithm consists of three core steps executed in each control cycle: singular-value screening and limiting (SVSL), generalized-distance-weighted extrapolation, and numerical solving of the air-gap regulation law. To assess its real-time capability, the algorithm was implemented on an FPGA-ARM co-processing platform (see Section 6). The FPGA is responsible for high-speed data acquisition, piecewise least squares fitting, and the numerical solver, while the ARM handles data storage and the user interface.

The measured execution time per control cycle was below 0.5 ms (for a sample window size $N = 20$), which is significantly shorter than typical industrial motor-control periods (1–10 ms). The computational complexity of the weighted extrapolation step is $O(N)$, and the numerical search along the constant-speed line converges within 3–5 iterations thanks to the monotonicity of the torque-gap characteristic. Therefore, the proposed method is fully feasible for high-speed, real-time applications such as soft start and power balance control in magnetic-coupler-driven systems.

6. Experiments

The experimental platform is shown in Figure 5. The maximum working speed of the speed-regulating magnetic coupler used in the experiment is 1500 r/min, where the rated power is 400 kW. An angle stroke electric actuator was made by Shenyang Research Institute of China Coal Technology and Engineering Group (Shenyang, China). Based on the operating conditions of the experimental platform and control requirements, using simulation methods and actual testing, the relationship between the air gap and the air-gap control quantity is

$$g = 34 - 30 \sin 0.0157u \tag{30}$$

where g is air gap, unit mm, u is the air-gap control quantity, and the value range is 0~100%. According to the above equation, the variation range of the coupler's air gap is 4~34 mm.

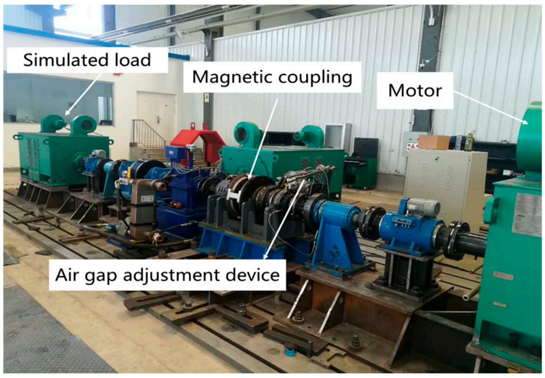

(**a**) Speed-regulating magnetic coupling

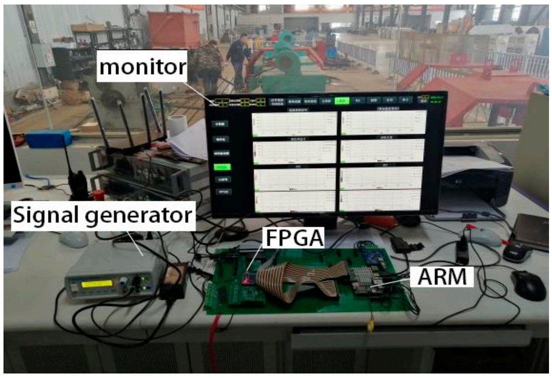

(**b**) Control system

Figure 5. Photo of speed-regulating magnetic coupling experiment platform.

EP4CE115F23I7N of Altera (San Jose, CA, USA) was selected as FPGA (Field-Programmable Gate Array). RK3399 of Rock chip (Fuzhou, China) was selected as ARM [Advanced RISC (Reduced Instruction Set Computer) Machine]. The Ubuntu 16.04 operating system (a Linux distribution) was installed on the RK3399 of Rock chip (Fuzhou, China) (a chip model code defined by the company's naming convention). FPGA was used for high-speed data interface and control algorithm. ARM was used for man–machine interface and data storage. Dual-port RAM and ring buffer technology were used. This enabled SPI (Serial Peripheral Interface) high-speed communication between FPGA and ARM.

Sample data are selected from historical data of air-gap control and output speed. The selected air-gap control amount and output speed should cover the whole working range of the coupler as far as possible. The variation curves of air-gap control and output speed over time are shown in Figure 6a and 6b, respectively.

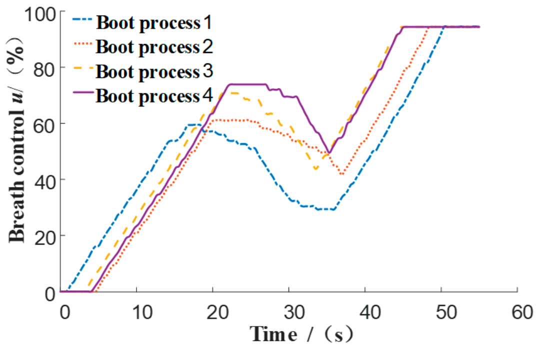

(**a**) The curve of air-gap control over time

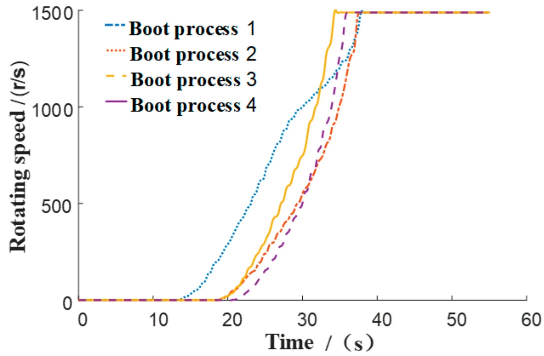

(**b**) Curve of output speed changing with time

Figure 6. Sample data curve.

According to Equations (11) and (13), the acceleration is calculated from the rotational speed time series. The result is shown in Figure 7, where SVSL is the abbreviation for singular-value limiting.

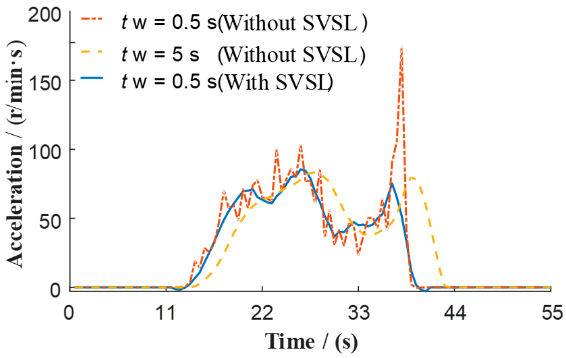

(**a**)

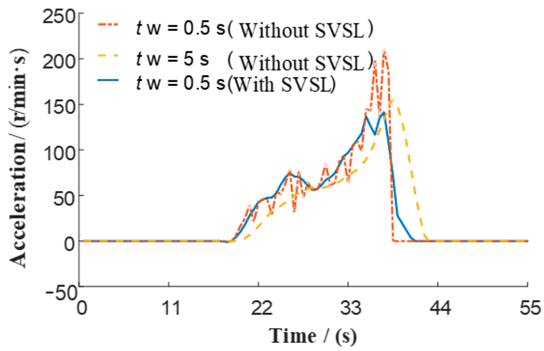

(**b**)

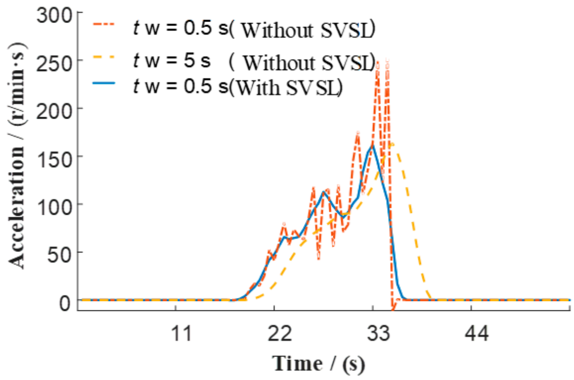

(**c**)

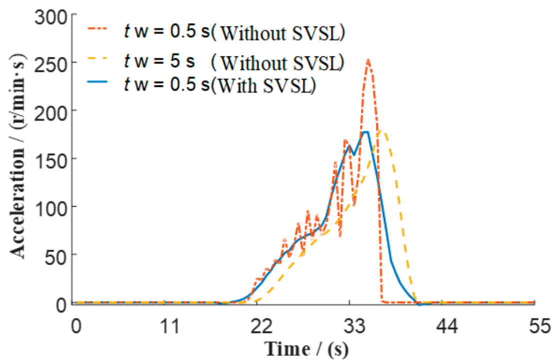

(**d**)

Figure 7. Calculation of trajectory angular acceleration by piecewise least squares method. (**a**) Raw angular acceleration sequence without processing. (**b**) Angular acceleration sequence after singular-value screening and limiting. (**c**) Angular acceleration estimation result under a wide time window. (**d**) Angular acceleration estimation result under a narrow time window combined with singular-value processing.

Figure 7 presents the angular acceleration results calculated using the piecewise least squares method. Figure 7a shows the raw fitted sequence, which exhibits significant noise and singular values. Figure 7b, after singular-value screening and limiting, shows a notable suppression of noise. Figure 7c, calculated with a wide time window, demonstrates strong noise suppression capability but also clear phase lag. Figure 7d, using a narrow time window combined with singular-value processing, improves estimation accuracy while ensuring real-time performance. The results indicate that the proposed SVSL algorithm can effectively achieve zero-phase-lag noise suppression and is suitable for high real-time control scenarios.

As shown in Figure 7, the wider the time window, the stronger the noise cancelation capability, but the greater the lag. Under normal circumstances, the singularity measure value of the signal is usually less than 1, and measure value at the singularity is greater than 1. Therefore, the singular-value threshold ρ is selected as 1.0 r/min*s. Through the singular-value limiter of (17), zero-phase filtering can be realized; that is, there is no phase lag while eliminating noise. Therefore, after using the SVSL algorithm, the angular acceleration can be calculated under a narrow time window to satisfy both signal accuracy and real-time performance.

By plotting the air-gap and speed values at the same time in Figure 6 on the $u-n$ plane, 4 sample trajectories can be obtained. Then, the angular acceleration calculation values of each point on the sample trajectory can be obtained from Figure 8. Thus, the acceleration intensity can be plotted in Figure 8. The four curves from left to right are the four sample trajectories in turn.

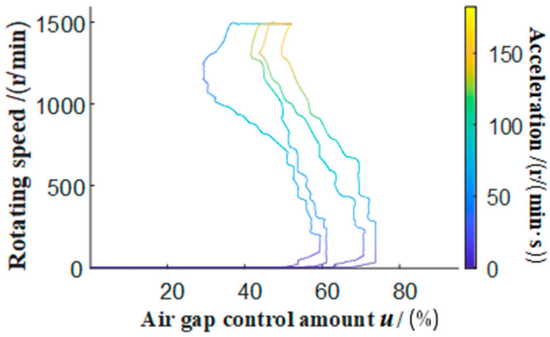

Figure 8. Acceleration intensity graph on sample trajectory.

According to (20) and (25), the angular acceleration on the trajectory in Figure 8 is extended to obtain the acceleration calculation value of the entire sample trajectory enclosed area. The generalized distance can be selected by $l_i = d_i^{\lambda}$, where λ is a positive real number.

The corresponding extension results when λ takes different values are shown in Figure 9.

From Figure 9, when λ is too small (generally $\lambda = 1, \lambda = 2$), the acceleration value calculated by the generalized distance weighting factor has an insignificant trend; when λ is too large ($\lambda \geq 4$), there is a jump in the calculated acceleration value; when it is moderate ($2 < \lambda < 4$), the calculated acceleration value is generally smooth and gradual. Therefore, this experiment chooses $\lambda = 2.5$.

Lyapunov coefficient η is selected as 1.5 in (7). The set speed is generated by the signal generator (orange dotted line in Figure 10). When using anti-singular data-driven control, the output speed is the blue line in Figure 10, where the air-gap regulation law is calculated according to the process in Figure 2. The output speed when using conventional PI control is the purple dotted line in Figure 10.

To quantitatively evaluate the repeatability and statistical performance of the control strategies, systematic comparative experiments were conducted on the test platform. The experimental design was as follows: while keeping the parameters of the proposed anti-singularity data-driven controller constant (Lyapunov coefficient $k = 1.5$, generalized distance parameter $\lambda = 2$), we randomly selected **8** distinct load points within the range of 70% to 100% of the rated load. At each load point, a complete setpoint speed tracking task, as shown in Figure 10, was executed once, constituting $N = 8$ independent trials. The relative mean square error (MSE) of speed tracking in each trial was recorded as the core performance metric.

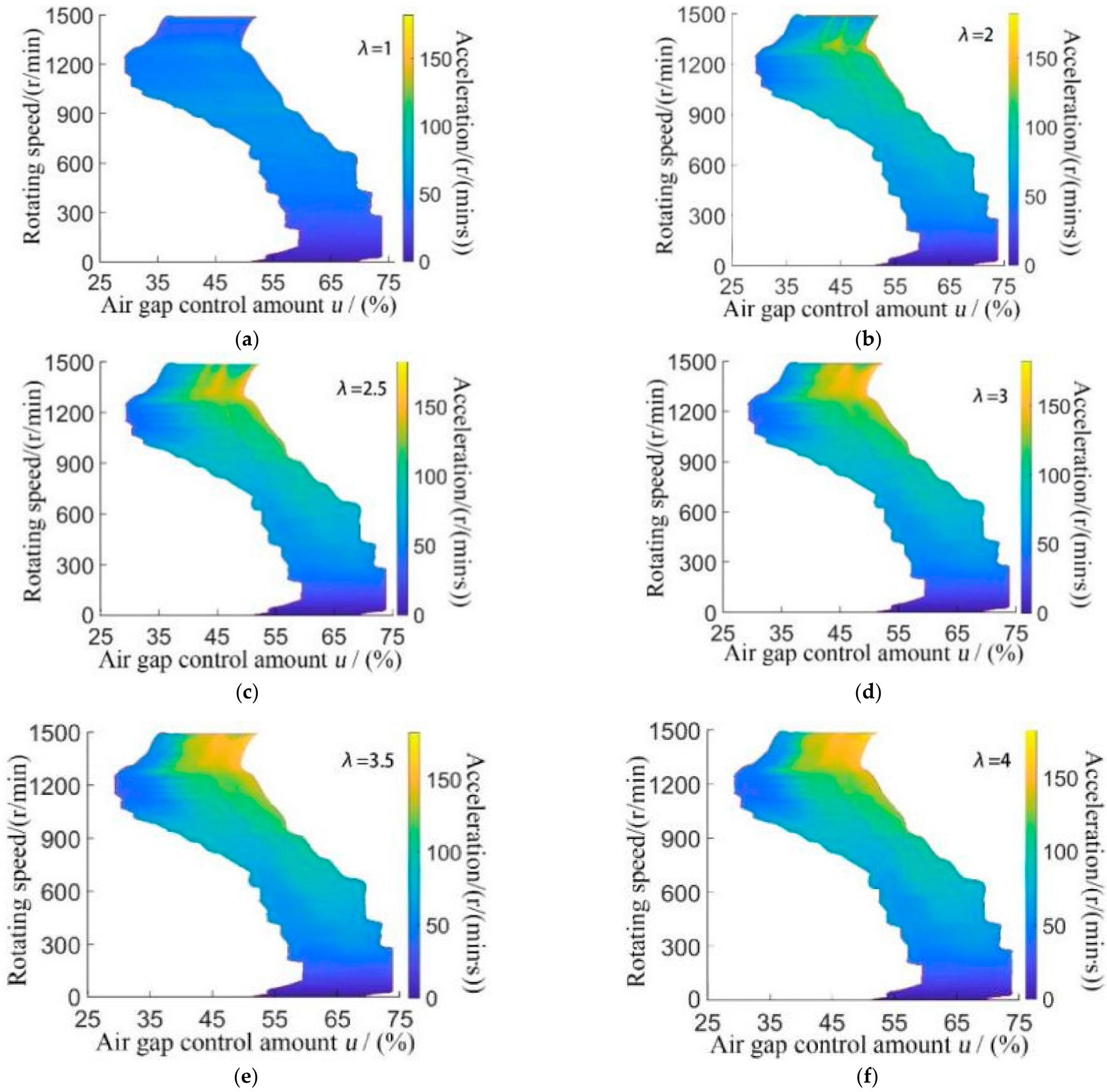

Figure 9. Angular acceleration intensity diagram around the trajectory. (**a**) Angular acceleration intensity diagram around the trajectory when $\lambda = 1$. (**b**) Angular acceleration intensity diagram around the trajectory when $\lambda = 2$. (**c**) Angular acceleration intensity diagram around the trajectory when $\lambda = 2.5$. (**d**) Angular acceleration intensity diagram around the trajectory when $\lambda = 3$. (**e**) Angular acceleration intensity diagram around the trajectory when $\lambda = 3.5$. (**f**) Angular acceleration intensity diagram around the trajectory when $\lambda = 4$.

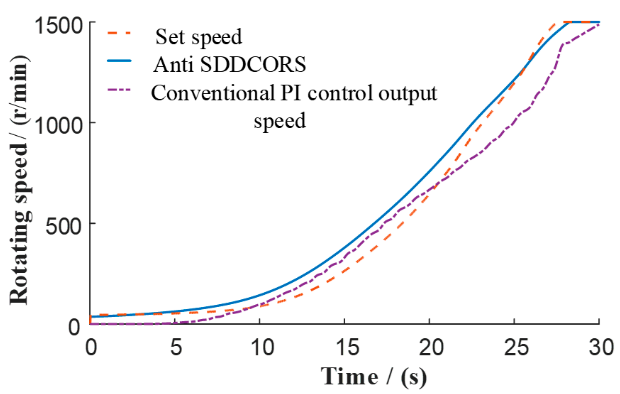

Figure 10. Speed deviation curve with time.

The statistical performance results of the two control methods are summarized in Table 3. The proposed method demonstrated superior and stable tracking performance across all 8 trials: the sample mean of its MSE was 3.15%, with a sample standard deviation of 0.52%. The calculated 95% confidence interval for the population mean is [2.71%, 3.59%]. This indicates that we can be 95% confident that the average tracking MSE under similar conditions lies within this interval. The maximum instantaneous tracking error did not exceed 4% in any trial. In contrast, the conventional PI controller under the same test conditions yielded an MSE mean of 7.82%, a standard deviation of 1.87%, and a 95% confidence interval of [6.29%, 9.35%], with its maximum error frequently exceeding 4%. A one-way analysis of variance (ANOVA) performed on the MSE data of the two independent sample groups revealed a highly significant between-group difference ($F(1, 14) = 57.3$, $p < 0.01$), providing strong statistical evidence that the proposed method offers significantly better control accuracy than the traditional PI control.

Table 3. Statistical summary of speed tracking performance (N = 8 independent trials).

Control Method	Mean MSE (%)	Std. Dev. of MSE (%)	95% CI for Mean (%)	Trials with Max Error < 4%
Proposed Method	3.15	0.52	[2.71, 3.59]	8/8
Conventional PI	7.82	1.87	[6.29, 9.35]	0/8

Note: One-way analysis of variance (ANOVA) performed on the mean MSE of the two trial groups indicates a statistically significant difference ($F(1, 14) = 57.3$, $p < 0.01$).

7. Analysis of Practical Engineering Applications

This method was applied to on-site high-efficiency and energy-saving transmission projects of permanent-magnet couplings in industries such as petroleum, steel, and coal mines, achieving precise control of motor soft start [23,24] and multi-machine power balance [25,26], ensuring the stable, reliable, and energy-saving operation of the equipment.

It is applied to the speed regulation of the booster pump drive in the petroleum field (as shown in Figure 11). Through data-driven control, it realizes the slow start of the permanent-magnet coupling under heavy load, effectively protecting the motor under strong impact load. The drive motor is started at the rated speed of 1500 r/min. Then, the coupling control system uses the proposed method to control the actuator. The air gap is slowly reduced via the speed regulation mechanism. The soft-start process begins. The loading motor will gradually increase its speed as the air gap decreases until it reaches the rated slip of 45 r/min of the coupling, that is, the loading motor speed is 1455 r/min. The soft-start process is completed, and the relevant data is extracted as shown in Figure 11.

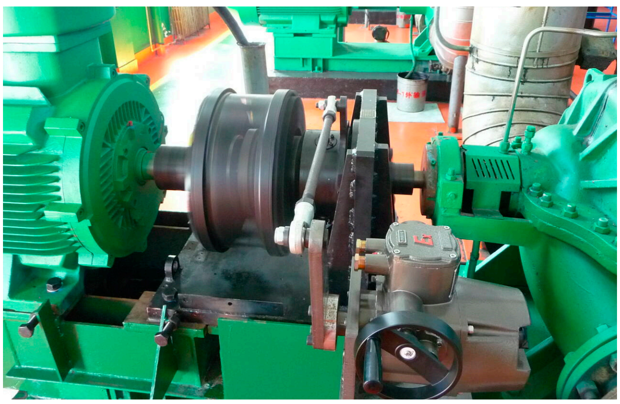

Figure 11. Application of permanent-magnet couplers in the petroleum industry.

To assess the repeatable performance of the soft-start strategy under practical operating conditions, we extracted data from $M = 6$ complete heavy-load soft-start processes across multiple field application cases (e.g., the booster pump drive scenario in the petroleum industry shown in Figure 11). These processes, corresponding to different initial load conditions and equipment states, can be considered representative independent samples. For each start-up process, its acceleration and total start-up time were analyzed.

The statistical results indicate that the soft-start process is smooth and controllable: the sample mean of the start-up acceleration is 0.12 m/s^2, with a sample standard deviation of 0.03 m/s^2. The 95% confidence interval is [0.09, 0.15] m/s^2, confirming that the start-up shock is strictly limited within the expected range ($\leq$0.15 m/s^2). The sample mean of the total start-up time is 25 s, with a standard deviation of 3 s, and a 95% confidence interval of [22.2, 27.8] seconds. These statistics demonstrate that the proposed S-curve tracking control strategy can stably achieve smooth, low-impact soft starts under varying field conditions, with controllable and consistent start-up times. As shown in Figure 12, it can be seen that the motor rotates with the input end of the coupling at the rated speed of 1500 r/min. As the load decreases with the reduction in the air gap, the speed gradually increases. Under the regulation of the control strategy, a gradual and slow start can be achieved. The starting acceleration can be controlled below 0.15 m/s^2, truly achieving soft start under load, avoiding faults such as excessive instantaneous inrush current and overload burnout of the motor caused by direct start and stop, and effectively protecting the motor.

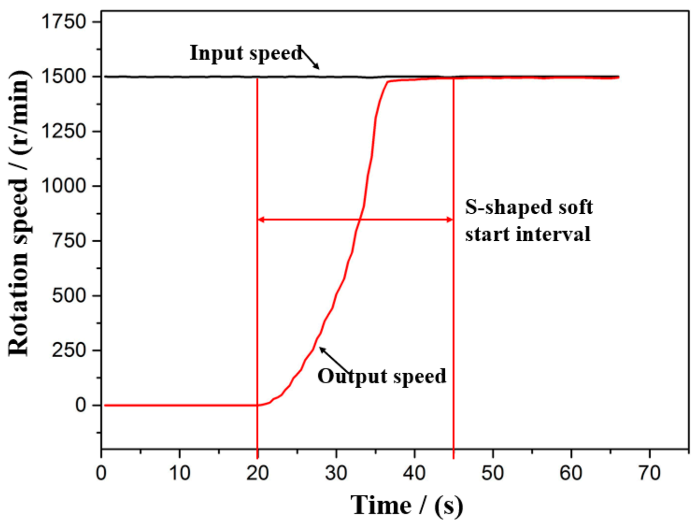

Figure 12. Changes in speed during soft-start control process.

It is applied to long-distance multi-machine drive belt conveyors and other load scenarios in coal mines. By precisely adjusting the air gap, it achieves power balance regulation between motors. On the one hand, it improves motor energy efficiency and achieves significant energy-saving effects. On the other hand, it also avoids problems such as belt breakage caused by different belt tensioning when motor output is uneven. For the multi-motor drive power balance function, we collected data from $k = 5$ typical power imbalance regulation cases (including different load distribution scenarios such as the 200–100 kW case mentioned in the text) in application settings like long-distance belt conveyors (Figure 13).

After applying the proposed distributed balance strategy in each case, the steady-state current imbalance among all drive motors (defined as the percentage of the maximum deviation of each motor's current from the average current) was recorded as the balance effectiveness metric. The current load power is 500 kW (generally, belt conveyors don't operate at full load). One motor outputs 200 kW based on the amount of coal on the belt, and the other outputs 100 kW. As a result, the two drive motors will have uneven output. The 200 kW motor may burn out when operating under heavy load. By precisely adjusting the air gap of the coupling through the anti-singular data-driven control method, the power balance regulation of the two drive motors is achieved, reducing the output power of the high-power motor and increasing that of the low-power motor. The current of both is pulled to the average current point to protect each motor and improve energy efficiency. Collect the currents of the two drive motors as shown in the figure (there are also load power scenarios such as 100–300 kW and 200–250 kW, as shown in Figure 14).

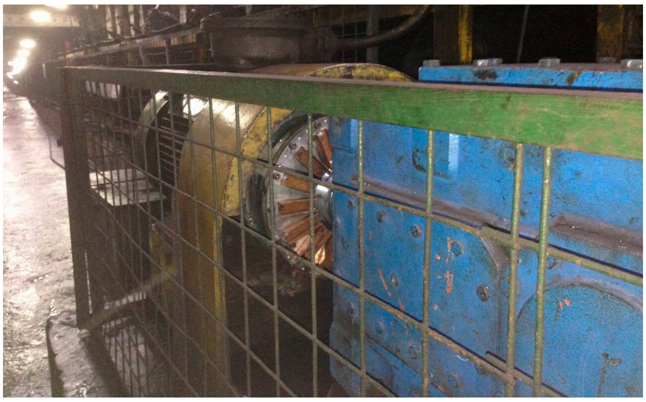

Figure 13. Application of permanent-magnet coupler in coal mining field.

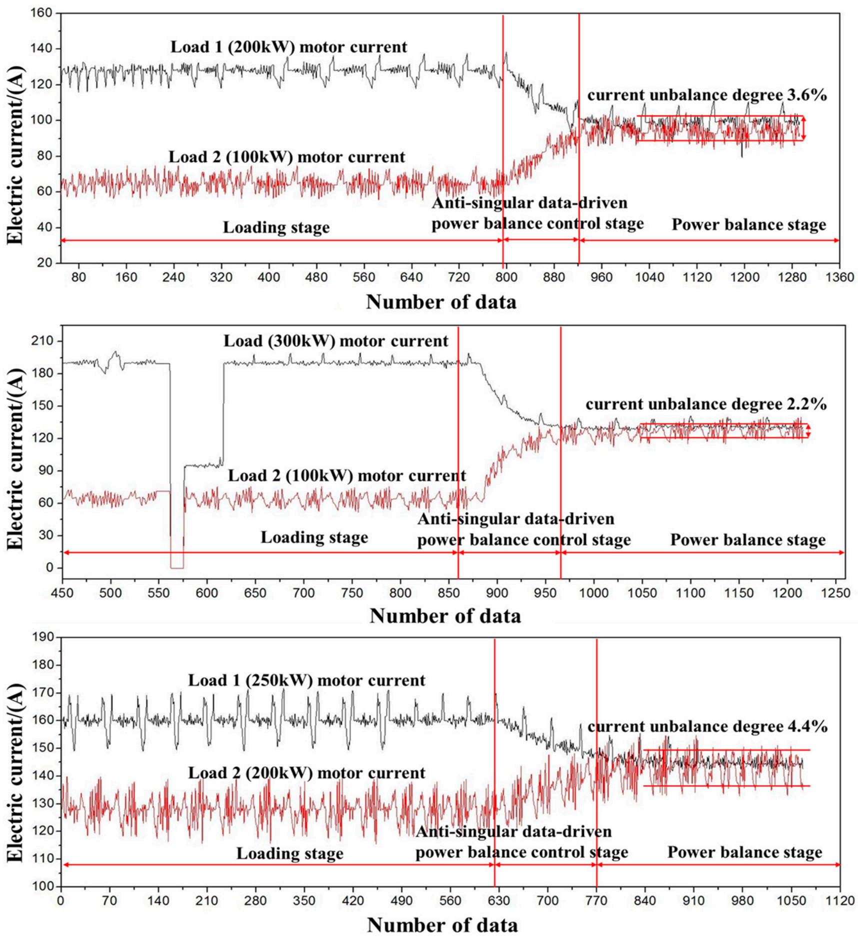

Figure 14. Current variation of multi-machine power balance control.

Statistical analysis shows that this strategy effectively achieves power balance: the sample mean of the current imbalance is 3.8%, with a sample standard deviation of 0.9%. The 95% confidence interval for the population mean is [2.7%, 4.9%]. This result aligns with the engineering goal of "current imbalance $\leq$ 5%" and provides a statistical precision range. Furthermore, by comparing the total system current (or power consumption) before and after applying the strategy, the average energy saving rate was calculated to be 17.6%, with a standard deviation of 2.1% and a 95% confidence interval of [15.1%, 20.1%]. This statistically verifies the significance and consistency of the energy efficiency improvement achieved through precise power balance. The average energy saving rate is 17.6%, with an annual electricity saving of 472,000 kilowatt-hours, equivalent to 179.36 tons of standard coal.

8. Conclusions

The magnetic coupler exhibits strong nonlinearity between torque, speed, and air gap. Based on Lyapunov stability theory, the air-gap regulation law equation was derived. Based on the time series of speed data, the angular acceleration of $u - n$ plane sample trajectory was calculated by piecewise least squares method. The amplitude intensity diagram and the phase intensity diagram were obtained, and the relationship between the frequency characteristics of the algorithm and the time-window width was analyzed. Based on the calculation of singularity measure of data points, the singularity screening and limiting were realized, and the anti-singularity of the system was improved. An epitaxial algorithm based on a generalized distance weighting factor is proposed to extend the rotational acceleration of $u - n$ plane sample orbit line to the entire orbit area of the sample, thus obtaining the data model. Using the angular acceleration value of the area surrounded by the sample trajectory, the air-gap adjustment amount is obtained by numerical solution.

Experimental data show that the error is within 4%. When applied to actual engineering sites, through the anti-singular data-driven control method, the precise adjustment of the air-gap quantity is achieved, realizing the functions of soft start and multi-machine power balance regulation. The soft-start time is approximately 25 s, and the start acceleration can be controlled below $0.15\ \mathrm{m/s^2}$. The unevenness of the multi-machine current is $\leq$5%, saving 17.6% of energy.

While the proposed anti-singularity data-driven control method demonstrates advantages in multiple aspects, it also has certain limitations, which point to directions for future research. Future work will focus on enhancing the online adaptability of the data model. A significant direction is to investigate safe and efficient online learning mechanisms, enabling the system to dynamically incorporate verified, high-quality new data points into the sample set during operation. This would allow the model to adapt to slow drifts in equipment characteristics or explore more optimal operating points, achieving true lifelong learning and performance evolution.

Author Contributions: Conceptualization, Y.Z. and C.Y.; methodology, Y.Z. and H.Z.; software, H.L.; validation, Y.Z., W.L. and H.Z.; formal analysis, Y.Z.; investigation, C.Y.; resources, H.Z. and H.L.; data curation, Y.Z.; writing—original draft preparation, Y.Z.; writing—review and editing, W.L.; visualization, H.L.; supervision, W.L.; project administration, W.L.; funding acquisition, Y.Z. All authors have read and agreed to the published version of the manuscript.

Funding: This work was supported by the Key Research and Development Program of Liaoning Province, China [Grant No. 2024JH2/102400022].

Data Availability Statement: All data analyzed or generated during this study are included in this article. The supporting data can be found within the article.

Conflicts of Interest: Hongju Zhao, Chuang Yang and Hao Liu were employed by Middling Coal Science and Industry Robot Technology Co., Ltd. The remaining authors declare that the research was conducted in the absence of any commercial or financial relationships that could be construed as a potential conflict of interest.

References

1. Wang, J.; Wang, D.; Wang, S.; Tong, T.; Sun, L.; Li, W.; Kong, D.; Hua, Z.; Sun, G. A Review of Recent Developments in Permanent Magnet Eddy Current Couplers Technology. *Actuators* **2023**, *12*, 277. [CrossRef]
2. Kim, H.; Chang, H.; Shim, H. Evaluating MR-GPR and MR-NN: An Exploration of Data-driven Control Methods for Nonlinear Systems. *Int. J. Control. Autom. Syst.* **2024**, *22*, 2934–2941. [CrossRef]
3. Fan, X.; Zhang, C.H.; Jiang, W.J.; Shen, J.J. Application of disc-type asynchronous permanent magnet coupling in double-drive coal belt conveyor. *Mech. Electr. Inf.* **2024**, *6*, 54–58. [CrossRef]
4. Liu, K.; Gao, H.; Hu, G.; Cui, H. Experimental and Theoretical Analysis of Magnetic-Thermal-Mechanical Coupling of Permanent Magnet Coupling. *AIP Adv.* **2024**, *14*, 095323. [CrossRef]
5. Cao, Z.; Mao, J.; Zhang, C.; Cui, C.; Yang, J. Safety-Critical Generalized Predictive Control for Speed Regulation of PMSM Drives Based on Dynamic Robust Control Barrier Function. *IEEE Trans. Ind. Electron.* **2025**, *72*, 1881–1891. [CrossRef]
6. Ling, L.; Huang, S.-D.; Cao, G.-Z.; Qiu, H. Comparison Analysis on Control-Increment-Based and Control-Quantity-Based Predictive Controls of Permanent Magnet Synchronous Motors. In Proceedings of the IEEE International Conference on Predictive Control of Electrical Drives and Power Electronics (PRECEDE), Wuhan, China, 16–19 June 2023; pp. 1–6. [CrossRef]
7. Zhou, Z.; Wang, J.; Zhang, S. Speed Synchronization Control Strategy of Dual-Motor System with Explicit Model Predictive Control. *IEEE J. Emerg. Sel. Top. Power Electron.* **2024**, *12*, 2787–2798. [CrossRef]
8. Moin, H.; Shah, U.H.; Khan, M.J.; Sajid, H. Fine-Tuning Quadcopter Control Parameters via Deep Actor-Critic Learning Framework: An Exploration of Nonlinear Stability Analysis and Intelligent Gain Tuning. *IEEE Access* **2024**, *12*, 98695–98710. [CrossRef]
9. Chen, M.; Li, X.; Han, Y. Current Control for PMSM Based on Data-Driven Control. In Proceedings of the International Conference on Computer and Communications (ICCC), Chengdu, China, 10–13 December 2021; pp. 1378–1382. [CrossRef]
10. Liu, Y.; Zhou, G.; Guo, L.; Sun, Z. ESO-Based Direct Model-Free Adaptive Predictive Compensation Control for Permanent Magnet Synchronous Motors. *IEEE Access* **2025**, *13*, 7837–7849. [CrossRef]
11. Wu, Y.; Meng, D. Data informativity for tracking control of learning systems: Test and design conditions. *Automatica* **2025**, *171*, 111885. [CrossRef]
12. Chen, D.; Lu, T.; Li, G. A survey of methods for handling initial state shifts in iterative learning control. *Heliyon* **2023**, *9*, e22492. [CrossRef]
13. Brosch, A.; Hanke, S.; Wallscheid, O.; Böcker, J. Data-Driven Recursive Least Squares Estimation for Model Predictive Current Control of Permanent Magnet Synchronous Motors. *IEEE Trans. Power Electron.* **2021**, *36*, 2179–2190. [CrossRef]
14. Lu, X.Y.; Hou, Z.S. Model free adaptive control with disturbance rejection based on modified Kalman filter. *Control Theory Appl.* **2022**, *39*, 1211–1218. [CrossRef]
15. Chen, J.; Yu, X.; Fang, J.; Wu, Z. A Model-Free Adaptive Iterative Learning Control for PMLSM. In Proceedings of the IEEE 14th Data Driven Control and Learning Systems (DDCLS), Wuxi, China, 22–24 May 2025; pp. 1712–1716. [CrossRef]
16. Hao, Y.; Zhao, Y. Research on coupling control of multiple permanent magnet synchronous motors based on NAISMC and SMDO. *PLoS ONE* **2023**, *18*, e0292913. [CrossRef] [PubMed]
17. Zhang, Z.; Wen, C.; Song, Y.; Feng, G. Adaptive Quantized Output Feedback Control of Nonlinear Systems with Mismatched Uncertainties and Sensor Failures. *IEEE Trans. Autom. Control* **2023**, *68*, 8216–8223. [CrossRef]
18. Ji, H.; You, Y.; Liu, S.; Wang, L.; Wang, W. A Novel Model-Free Adaptive Recursive Optimal Control for Time-Varying Nonlinear Systems. In Proceedings of the IEEE 13th Data Driven Control and Learning Systems Conference (DDCLS), Kaifeng, China, 17–19 May 2024; pp. 690–695. [CrossRef]
19. Yang, W.; Li, S.; Luo, X. Data driven vibration control: A review. *IEEE/CAA J. Autom. Sin.* **2024**, *11*, 1898–1917. [CrossRef]
20. Zhou, Q.; Shi, K.; Xu, K.; Du, G.; Gao, K. Optimized Multi-Motor Power Control Strategy for Distributed Permanent Magnet Direct Drive Belt Conveyors. *Appl. Sci.* **2024**, *14*, 8343. [CrossRef]
21. Sun, Z.; Xu, S.; Ren, G.; Ma, G.; Chi, M. Dual-mode Model Predictive Control Strategy for Permanent Magnet Synchronous Traction Motor in the Full Speed Range. *Proc. CSEE* **2025**, *45*, 748–757. [CrossRef]
22. Zhang, X.; Ren, T.; Jin, G.; Tian, J.; Han, J. Review on fault diagnosis technology of permanent magnet synchronous machine. *Manuf. Technol. Mach. Tool* **2025**, *6*, 85–95. [CrossRef]
23. Fang, Y.; Gu, C.; Zhao, Y.; Wang, W.; Guan, X. Smooth trajectory generation for industrial machines and robots based on high-order S-curve profiles. *Mech. Mach. Theory* **2024**, *201*, 105747. [CrossRef]
24. Verkroost, L.; De Smet, J.; Vancampenhout, R.; De Belie, F.; Sergeant, P. Multi-Agent Control Scheme for Power Distribution in a Multi-Three-Phase Motor Drive Fed by a Stacked Polyphase Bridges Converter. *IEEE Trans. Energy Convers.* **2024**, *39*, 2568–2580. [CrossRef]

25. Wen, L.; Liang, B.; Li, B.; Zhang, L. Power Balance Control Strategy of Permanent Magnet Synchronous Motor of Belt Conveyor. *IEEE Access* **2022**, *10*, 117045–117052. [CrossRef]
26. Yan, W.; Lu, W.; Jiang, Z.; Zhao, Y.; Wang, W.; Wang, Y.-C. Current Control of Electrolytic Capacitor-Less Variable Frequency Drive System for Synchronous Reluctance Motors Based on Power Balancing and Compensation. *IEEE Access* **2024**, *12*, 150639–150650. [CrossRef]